

# Fluorine spillover for ceria- vs silica-supported palladium nanoparticles: a MD study using machine learning potentials

Da-Jiang Liu<sup>1</sup> and James W. Evans<sup>1,2</sup>

<sup>1</sup>*Division of Chemical & Biological Sciences, Ames National Laboratory – USDOE, Ames, Iowa 50011 USA*

<sup>2</sup>*Department of Physics & Astronomy, Iowa State University, Ames, Iowa 50011 USA*

(\*Electronic mail: Author to whom correspondence should be addressed: dajiang@ameslab.gov)

(Dated: 14 June 2023)

Supported metallic nanoparticles play a central role in catalysis. However, predictive modeling is particularly challenging due to the structural and dynamic complexity of the nanoparticle, and of its interface with the support, and given that sizes of interest are often well beyond that accessible via traditional *ab initio* methods. With recent advances in Machine Learning, it is now feasible to perform MD simulations with potentials retaining near-DFT accuracy which can elucidate the growth and relaxation of supported metal nanoparticles, as well as reactions on those catalysts, at temperatures and time scales approaching those relevant to experiments. Furthermore, surfaces of the support materials can also be modeled realistically through simulated annealing to include effects such as defects and amorphous structure. We study adsorption of fluorine atoms on ceria and silica supported palladium nanoparticles using machine learning potential trained by DFT data using the DeePMD framework. We show defects on ceria and Pd/ceria interfaces are crucial for initial adsorption of fluorine, while the interplay between Pd and ceria and the reverse oxygen migration from ceria to Pd controls spillover of fluorine from Pd to ceria at later stages. In contrast, silica supports do not induce fluorine spillover from Pd particles.

## I. INTRODUCTION

It has long been speculated that catalyst supports often participate actively in heterogeneous catalysis rather than acting as inert bystanders merely providing a high surface area material on which catalysts are dispersed. One of the ways that supports can participate in the reaction is through spillover of adsorbate species from the metal catalyst to the support.<sup>1-3</sup> Theoretical studies of spillover are currently being pursued, but mostly for carbon supports.<sup>4-6</sup> To date, studies of metal oxide supports are more limited.<sup>5,7</sup> This is due to the inherent complexity of the systems, where the structure of the oxide support, the interface between the catalyst and support, and the shape and structure of the catalyst nanoparticles, all provide challenges for modeling. In addition, it is necessary to realistically describe adsorption and diffusion of chemisorbed reactant species in these complex systems.

Metallic nanoparticles supported on oxides, as well adsorption and reaction on these nanoparticles, provide a distinctive challenge for computational studies.<sup>8</sup> Their sizes are often too large for direct *ab initio* calculations, but too small for more phenomenological coarse-grained continuum modeling. Also, the need to treat a combination of transition metal, oxide, and chemical reactions makes the development of effective empirical potentials difficult. Machine learning naturally provides an enticing new approach to the problem, and there are some new developments in applying machine learning to the general problem of nanoparticles, supported or unsupported.<sup>9-11</sup> It should, however, be noted that other phenomenon such as morphological evolution for larger metal nanoparticles on time scales up to minutes or longer are best addressed via stochastic modeling ideally incorporating a realistic description of surface diffusion kinetics.<sup>12-14</sup>

Recent advances in development of machine learning

potentials<sup>15-19</sup> make molecular dynamics (MD) simulations feasible for up to thousands of atoms and for up to a few nanoseconds. In this contribution, we will demonstrate that simulations at a size and time scale achievable through machine learning potential can facilitate answering many questions for heterogeneous catalysis on supported metal nanoparticles. Using fluorine adsorption on ceria and silica supported Pd nanoparticles as an example, we develop simulation methods that can be used to study the structure of the oxide support (Sec. III), size and shapes of the supported catalyst nanoparticles (Sec. IV), and adsorption and migration of reactants on supported nanoparticles as well as spillover to the supports (Sec. V). General methodology for using DeePMD to train ML potential from DFT data is given in Sec. II and conclusion is given in Sec. VI.

## II. DEVELOPING GENERAL POTENTIALS FOR HETEROGENEOUS CATALYSTS

### A. Training

Some aspects of the methodology and code development have already been reported previously.<sup>20,21</sup> Plane-wave density-functional theory (DFT) calculations were performed using the VASP code,<sup>22</sup> with Perdew-Burke-Ernzerhof (PBE)<sup>23</sup> functional and the recommended PAW potentials released with VASP 5.4. The energy cutoff is 400 eV for all elements. The extraction of energy and forces, training to an artificial neural network with the *se\_e2\_a* descriptor were performed using the DeePMD-kit (v2.1.5) software.<sup>24</sup> MD simulations and data analysis were performed with Python, heavily relying on the atomistic simulation environment (ASE).<sup>25</sup> MD simulations are mostly performed using constant NVT (canonical ensemble) and the the temper-

ature is controlled by a fluctuation Langevin force and equilibrated by a friction force with coefficient of 0.002. The time step is 2 fs for systems where the lightest element is O, and 5 fs for systems where the lightest element is F.

Through trial and error, we have formulated some guidelines for efficient development of machine learning potentials from *ab initio* data for systems involving nanoclusters and surfaces. We train individual potentials for all combinations of relevant elements. For example, for the fluorine adsorption on ceria supported palladium particle, potentials for Ce, F, O, Pd, CeF, CeO, CePd, FO, ..., CeFOPd, are all developed, instead of just a single potential for CeFOPd. This is because it is much more efficient to perform calculation using the potential tailored to individual components, also they are generally more accurate with same amount of training. Although strictly speaking, potentials developed for individual components do not give exactly the same result as the potentials for more complete systems, they are generally close enough not to cause any physical problem. For example, structure minimized using the potential for smaller systems will also be stable using potential for the larger system. This is also related to the feature that the library of DFT data is shared between all components, so that DFT results for Pd are also used for training of potential for PdO, CePd, CeOPd, etc.

The generation of DFT data is an iterative process. The initial configuration for training is generally a nanocluster consisting of the relevant elements. In cases where there is a common and stable bulk phase for those elements, such as fcc for the single element Pd, we choose it as the starting point. Otherwise, we search for the densest phase from the Material Project.<sup>26</sup> Nanoclusters with side lengths around 1.3 nm are placed in a cubic supercell with twice the volume so that they are allowed to expand and/or melt at 3000 K, simulated for 2000 time steps using the VASP code. Note that we use a single  $\Gamma$   $k$ -point, and so tend to choose supercells of at least 1.5 nm in side length. The results are then used for training the initial ML potential. Using Pd as an example, we first create a cubic Pd nanocluster with 108 atoms and place it in a cubic supercell with 1.5 nm cell length. We perform DFT MD simulations at 3000 K for 2000 time steps or 10 ps. The initial ML potential is obtained by training these DFT data for  $10^5$  training steps. We then create another system of 256 Pd atoms with the fcc structure in a supercell with periodic boundary condition with the equilibrium volume  $(15.8 \text{ nm})^3$ . The system is then simulated using the ML potential at 4000 K, while gradually increasing the supercell size from 1.58 nm to 1.6 nm for another 2000 time steps (10 ps) (this slight increase in volume is optional, it is used here for ease of systematically adjusting the volume when the need of additional densities arises). The resulting configuration is then used as the starting point for another DFT simulation at the same temperature. The new DFT data, combined with the old data, is used to train a new ML potential. We then use this ML potential to simulate the 256 Pd atoms system at 4000 K, but this time compress it to a supercell with size length 1.4 nm, so that density is about 1.43 times the equilibrium value. We then simulate this denser structure with DFT, and then combine the new data to train a new ML potential. We find that it is important to vary the density of

the system to obtain a ML potential with general applicability, not just for the equilibrium bulk system. Even though as a whole system, the palladium system will not reach a density as high as 1.4 times the equilibrium volume under normal conditions, the ability to model correctly much shorter bond lengths than the equilibrium value is important for describing defects at step edges and kink sites.

We find in general, after three iterations, a model with no obvious pathologies can be obtained. Under conditions of normal temperature and pressure, the ML potential does not give catastrophically wrong answer. Results can be considered generally acceptable for instructive purpose. However, for more serious applications, further refinements and additional validation are often necessary. For a specific application of the ML potential, we perform DFT calculations first on a system of reasonable size achievable by DFT, generally started with a configuration obtained by simulations with ML potentials. We then compared the DFT results with the ML potential. For example, simulated annealing of Pd nanoparticles of 192 atoms was performed using the ML potentials, and configurations below and near the melting temperature (1000 K and 1500 K) are used for the initial configuration of further DFT simulations. If the rms errors for energy comparing DFT and ML potentials are too big (e.g., larger than 0.05 eV/atom), further training of ML potential are conducted using the new DFT data. In the case of Pd, we find the rms error is only 0.01 eV, even without further training. Most systems, however, do require additional training and further iterations.

## B. Validation

Methodology for systematic validation of the ML potentials is still in development. At this stage, much of the validation relies on our own physical and chemical knowledge and intuition. We inspect manually results of MD simulations using ML potentials and compare with existing knowledge of the system. When a system behaves “strangely”, it is usually the consequence that the ML potential is exploring part of the PES that it is not trained. Additional DFT calculations are then performed, results of which are used for further refinement of the ML potential.

For a more quantitative assessment, we need to compare ML potentials with that of DFT calculations. Here we use a two-pronged approach. The first is an application specific approach. We use ML potentials to create systems that are expected to be encountered during the the specific application, such as pure Pd, ceria, and silica nanoparticles, ceria and silica supported Pd, and fluorine adsorbed on those nanoparticles. They are of sufficiently small sizes so that DFT calculations can be performed, results are compared with the prediction of the ML potentials.

Table I shows error estimates of two ML potentials used in this work for these selected systems. The RMSE for the total energy (per atom) and forces on each atom is obtained from 30 randomly selected configurations for each DFT MD simulation.

Accuracy of the ML potentials for these scenario is the most

TABLE I. Errors estimates between selected ML potential and DFT calculations for application specific systems.

System	Temperature (K)	Error in energy (eV/atom)	Error in force (eV/Å)
ML potential for Ce-F-O-Pd			
Pd <sub>192</sub>	1000	0.0098	0.073
Ce <sub>72</sub> O <sub>144</sub>	1300	0.0035	0.25
Pd <sub>32</sub> /Ce <sub>72</sub> O <sub>144</sub>	800	0.0065	0.16
F <sub>36</sub> Pd <sub>36</sub> /Ce <sub>72</sub> O <sub>144</sub>	800	0.023	0.23
ML potential for F-O-Pd-Si			
Pd <sub>192</sub>	1000	0.012	0.072
Si <sub>72</sub> O <sub>144</sub>	3000	0.0095	0.25
Pd <sub>32</sub> /Si <sub>72</sub> O <sub>144</sub>	800	0.0062	0.19
F <sub>64</sub> Pd <sub>38</sub> /Si <sub>72</sub> O <sub>144</sub>	800	0.012	0.33

important specific to our applications. However, it may not be an accurate gauge for their general applicabilities. In fact, the choice of the training data set inevitably reflects the desired application due to the nature of our iterative procedure, so the training is biased towards these applications. To provide a more unbiased assessment, we conduct more systematic tests. First, we fill up randomly a simulation box with atoms of each element sequentially. The system is equilibrated at 1600 K for 2000 time steps between each addition of atoms by performing MD simulations using the ML potentials. The resulting configurations are then used as the starting point for DFT MD simulations for another 200 to 2000 time steps. The DFT trajectories are then compared with ML potentials. The equilibration using the ML potentials versus purely randomly filling the cell with atoms serves two important considerations: firstly it allows us to validate the most energetically favorable part of the ML PES, secondly, assuming the ML potential is reliable, it allows us to focus on the physically meaningful part the PES. There is no need to model the unphysical part of the PES very accurately.

Table II summarizes the RMSE errors in energy/atom and forces for various randomly synthesized systems using above described procedures. As expected, the errors for random systems are generally larger than those for application-specific systems. There are some variances, such as agreement for pure Pd system is much better than for Ce, perhaps reflecting the facts that there are more extensive DFT for Pd system than Ce. Fortunately, it is in line with our application, since we expect to see pure Pd nanoparticles, but not pure Ce nanoparticles in our system. For systems that do involve pure Ce, naturally more DFT data for Ce should be generated.

A more physical illustration of the validness of the ML potential can be represented by the comparison of the compositional formation energy between DFT and ML potential. Results for selected pairs of elements are shown in the supplementary material.

TABLE II. Errors estimates between selected ML potential and DFT calculations for synthesized systems by randomly depositing 32 atoms of each species in a (1.5nm)<sup>3</sup> cell with periodic boundary conditions, equilibrated at 1600 K.

System	Error in energy (eV/atom)	Error in force (eV/Å)
ML potential for Ce-F-O-Pd		
Ce	0.122	0.26
F	0.075	0.17
O	0.014	0.33
Pd	0.008	0.11
Ce, F	0.070	0.28
Ce, O	0.060	0.27
Ce, Pd	0.024	0.15
F, O	0.040	0.57
F, Pd	0.027	0.33
O, Pd	0.009	0.32
Ce, F, O	0.014	0.35
Ce, F, Pd	0.009	0.18
Ce, O, Pd	0.011	0.19
F, O, Pd	0.036	0.36
Ce, F, O, Pd	0.017	0.19
ML potential for F-O-Pd-Si		
F	0.056	0.16
O	0.016	0.34
Pd	0.006	0.11
Si	0.018	0.32
F, O	0.055	0.41
F, Pd	0.024	0.30
F, Si	0.031	0.40
O, Pd	0.013	0.31
O, Si	0.030	0.45
Pd, Si	0.032	0.22
F, O, Pd	0.026	0.35
F, O, Si	0.020	0.40
F, Pd, Si	0.032	0.24
O, Pd, Si	0.015	0.31
F, O, Pd, Si	0.018	0.25

### III. MODELS FOR CERIA AND SILICA SUPPORTS

Ceria (CeO<sub>2</sub>) and silica (SiO<sub>2</sub>) are two common catalyst supports. The crystal structure of ceria and silica are well-studied and can be used to design the model surfaces for catalyst support. For example, it is known from DFT calculations that CeO<sub>2</sub>(111) surface is the most stable.<sup>27,28</sup> Thus, it is natural to study, e.g., catalytic properties, using the ideal CeO<sub>2</sub>(111) surface as the basis, but potentially also introducing defects such as oxygen vacancies using energy derived from DFT calculations<sup>29</sup> or from experiments.<sup>30</sup>

Here, we develop a methodology for preparing metal oxide surfaces using MD simulations with ML potentials that could be widely applicable for a variety of systems. For ceria, we start with a nanocube of Ce<sub>600</sub>O<sub>1200</sub> and raise the temperature to 3000 K at a rate of 25 K/ps using the ML potential, so that the precise starting configuration is not so relevant. We then put the nanoparticle in a 3.8 × 3.8 × 7.6 nm<sup>3</sup> supercell and gradually increase the supercell to a size of 4.8 × 4.8 × 9.6

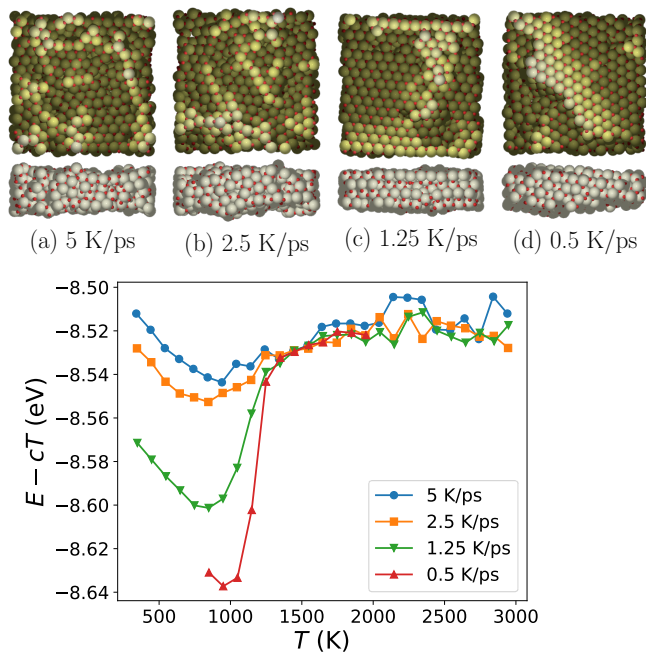


FIG. 1. (a)-(d) Top and side-views of  $\text{Ce}_{600}\text{O}_{1200}$  slabs cooled down to 800 K at various cooling rate from MD simulations using ML potential. Side views show both top and bottom surfaces of the ceria slab. Lower panel shows the energy per atom plot, where  $c$  is the specific heat averaged over 300K to 3000K from the simulations (usually from results with the fastest cooling rate, but the same number is used for all cooling rates so that comparisons between the plots are not distorted by the choice of  $c$ ) used to shift the plot making the transition near 1200 K more pronounced.

$\text{nm}^3$  at 3000 K in 10 ps. The nanoparticle dimension is sufficiently close to 3.8 nm that at this temperature and time scale, there are enough mobility for the ceria nanoparticle to bridge the simulation cell and given the periodic boundary conditions convert into a near flat slab. We then reduce system temperature at various cooling rates to 800 K, while maintaining the same supercell.

Figure 1 shows results of such a simulated annealing process for ceria. With faster cooling rate (above 1 K/ps), the system is not very ordered, with only short range hexagonal structure present. The surface consists of many single-atom-wide ridges. With slower cooling rate, the system becomes more ordered, with smooth facet of hexagonal surfaces. At the slowest cooling rate performed, a step structure is also present on the surface. The energy versus temperature plot has a clear signature of first-order transition corresponding to crystallization around 1200 K with the slower cooling rate. The feature that this is much lower than the usually cited 2700 to 2900 K bulk melting temperature for ceria is expected to be associated with effects of both small sizes and hysteresis in simulations, and does not necessarily indicate any deficiency of the ML potentials. For comparison, MD simulations of a homogeneous ceria system ( $\text{Ce}_{108}\text{O}_{216}$  in a cube with 16.40 Å side length and periodic boundary conditions) yield a melting temperature around 2800 K at a heating rate of 2.5 K/ps.

Silica of the type used as a catalyst supports is less

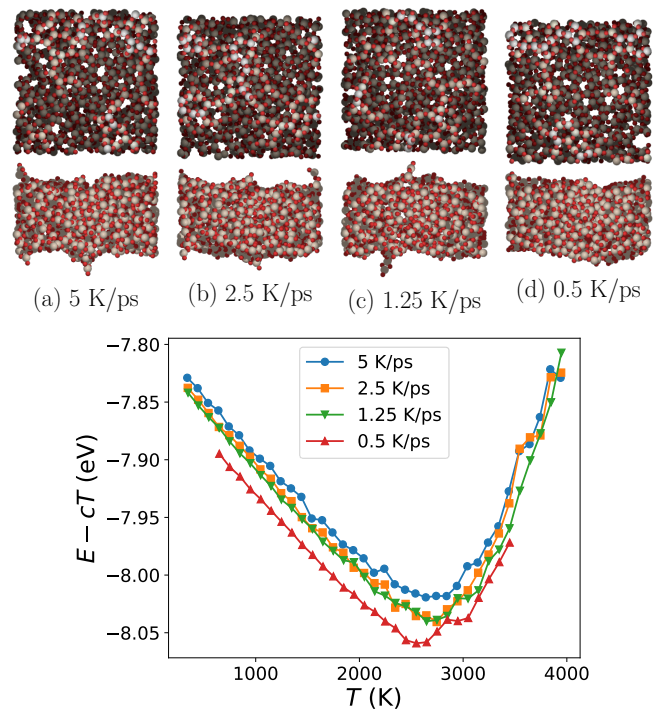


FIG. 2. Similar to Fig. 1, but for a  $\text{Si}_{576}\text{O}_{1152}$  system in a  $3.8 \times 3.8 \times 7.6 \text{ nm}^3$  supercell.

amenable to standard DFT analysis since the material is generally amorphous. Using a similar method as for ceria, Figure 2 shows results for simulated annealing of  $\text{SiO}_2$ . A slower cooling rate leads to a more stable structure. However, even at 0.5 K/ps, no ordered structure is found. There are signatures for latent heat in the  $E - cT$  versus  $T$  plots, but the transition is much further spread out and does not become obviously sharper as the cooling rate increases. Also the energy at lower temperatures are not as sensitive to the cooling rate, at least for the range simulated. Those are indicative to formation of amorphous silica, which is consistent with the observations that amorphous and glassy silica is a common product solidifying silica melt or from the sol-gel process, while crystallization requires more carefully controlled cooling. MD simulations have long been used to study amorphous silica, but mostly using empirical potentials.<sup>31</sup> However, recently, machine learning potentials have started to compete with empirical potentials.<sup>32</sup>

#### IV. FORMATION OF PALLADIUM NANOPARTICLES ON MODEL CERIA AND SILICA SURFACES

After preparing model ceria and silica surfaces, we can now model supported Pd nanoparticles. One could consider the following two approaches to describe this process. The simpler one is to directly place a preformed Pd nanoparticle on the surface of the support, then study the evolution of its shape and structure due to interaction with the support using MD simulations. The other approach is to simulate impreg-

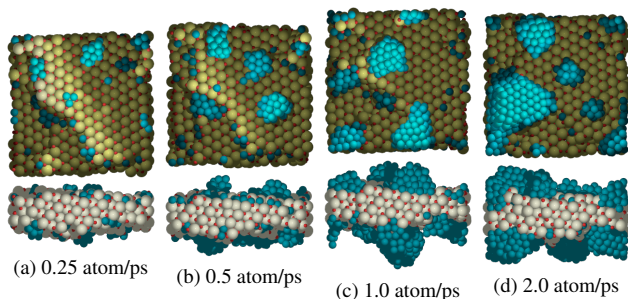


FIG. 3. Top and side views of Pd nanoparticles which are formed on both sides of a  $\text{CeO}_2$  slab with deposition rates 0.25, 0.5, 1.0, 2.0 atoms/ps in (a)-(d), respectively, after 1.024 ns. Simulations are performed at 800 K and in a  $4.8 \times 4.8 \times 9.6 \text{ nm}^3$  cell with periodic boundary conditions. Pd atoms that are not attached to support are deleted from the picture.

nation of the support with Pd precursors via incipient wetness followed by calcination and reduction, as often utilized in experiments.<sup>21</sup>

While the second approach is beyond our current capabilities, we develop a methodology that mimics the formation of metal nanoparticles (although on much shorter times scales), and which thus can be used to systematically explore this process. We assume individual free Pd atoms spontaneously emerge through reduction during the formation process. For Pd/ $\text{CeO}_2$ , we use the model system obtained in Sec. III (also see Fig.1) by cooling to 800 K with the slowest cooling rate. Pd atoms are randomly placed in the  $4.8 \times 4.8 \times 9.6 \text{ nm}^3$  simulation cell, with the condition that new atom is at least 0.3 nm away from any existing atoms. One of the parameters that can be adjusted is the rate that Pd atoms added to the simulations. In principle, this should be a stochastic process that occurs randomly throughout a simulation. However, for simplicity, in this work we just add a fixed number of Pd atoms for every 4 ps of simulations.

Figure 3 shows results of simulations with different Pd deposition rates after 1.024 ns of simulations at 800 K. Most of the Pd islands have a semi-spherical shape, but some of them are triangular or trapezoidal. Those more exotic shapes are due to the merging of smaller islands and represent transient configurations during a reshaping process.

Figure 4 show the results for the formation of Pd islands on a silica support. A smaller  $3.8 \times 3.8 \times 7.6 \text{ nm}^3$  cell is used here but containing approximately the same amount of atoms as the ceria. We observe a higher mobility of Pd nanoparticles compared with ceria. This feature is consistent with the observation that the shape of Pd nanoparticle is more spherical. The smaller contact area with the support indicates weaker binding between Pd and silica than for ceria, which correlates with higher mobility.

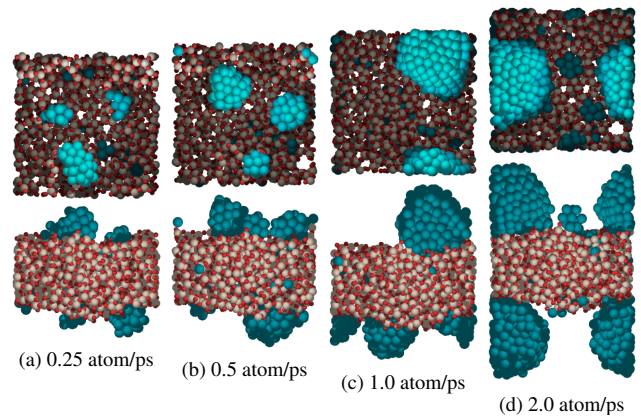


FIG. 4. Same as Fig.3, but with  $\text{SiO}_2$  support, after 512 ps and in the  $3.8 \times 3.8 \times 7.6 \text{ nm}^3$  simulation cell.

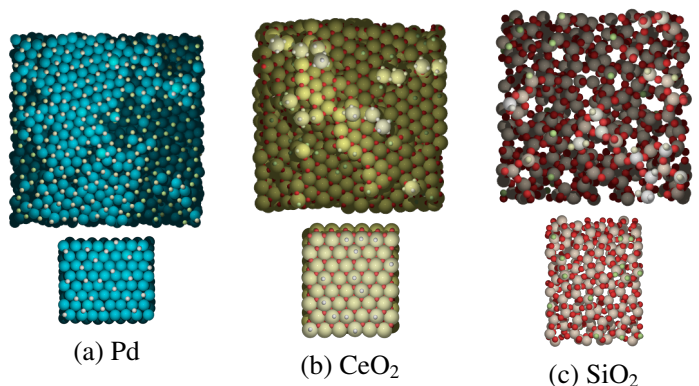


FIG. 5. Sample of configurations of F adsorption simulated at 800K on models for (a) Pd, (b) ceria, and (c) silica substrates. Top panels: using substrates annealed from melt. Bottom panel: using crystalline Pd(111),  $\text{CeO}_2(111)$ , and  $\alpha$ -quartz(0001) with  $(2 \times 1)$  reconstruction.

## V. FLUORINE ADSORPTION ON CERIA AND SILICA SUPPORTED Pd NANOPARTICLES

### A. Fluorine adsorption on Pd, on ceria, and on silica

Before we present results of fluorine adsorption on the supported Pd catalyst nanoparticles, we briefly discuss results for fluorine adsorption separately on each of the components (on Pd, on ceria, and on silica). We perform MD simulations using the same method as in Sec. IV for Pd, but now instead using F atoms. This is not intended to simulate any particular reaction, but rather to provide a generic picture of F adsorption.

The prepared model Pd slab has a (111) surface orientation, with a Pd island on one side of the slab. At low F dosage, F adatoms occupy 3-fold sites. At the elevated temperature of 800 K, no preference to step edges is observed. As the coverage of F increases, the surface consists of a large semi-ordered Pd-F structure and smaller Pd-F complexes that scattered on the lower terrace [see Fig. 5(a)]. At even higher dosage, pal-

ladium fluoride grows in height and become 3D islands.

For fluorine adsorption on ceria, we observe that F preferentially adsorbs at the step edge at low coverage. Some of the Ce atoms at kink sites can have two F atoms attached. As F coverage increase, more and more Ce atoms detach from the step edges and have multiple F atoms attached to them. Those  $CeF_x$  units can also form small Ce-F complexes, but no large ordered surface cerium fluoride is observed. At much larger F coverage,  $CeF_x$  molecules start to detach from the surface (at 800 K).

Fluorine adsorption on the model amorphous silica is much harder to characterize, with no obvious stages. It can be generally described as competition of fluorine with oxygen to form bond with silicon atoms. Unlike oxygen, silicon and fluorine do not form any complex network. Finally, at very high F coverage,  $SiF_x$  molecules also start to detach from the surface.

Some quantitative analysis can be performed on the MD simulation results. By measuring the change in potential energy as the number of F atoms increases, we can deduce the heat of adsorption and use it as the adsorption energy for fluorine adatoms. Using the energy (per atom) of a  $F_2$  dimer in the gas phase as the reference, the fluorine adsorption energy on a clean surface is estimated to be  $-2.4$  eV for Pd,  $-2.5$  eV for ceria, and  $-1.5$  eV for silica. A more negative energy means a stronger preference for F to attach to the surface. Note that on a flat  $CeO_2(111)$  surface, the adsorption energy is only  $-1.6$  eV from our MD simulations, so defect sites are crucial for understanding the catalytic properties of ceria supports. On the other hand, we also study the fluorine adsorption on a  $\alpha$ -quartz(0001) surface with no defects and no dangling bonds. A similar adsorption energy of  $-1.5$  eV is obtained for low F coverage as for the model silica slab analyzed above. The F adsorption energy on a flat Pd(111) surface is  $-1.9$  eV from MD simulations.

## B. Fluorine adsorption on ceria-supported palladium nanoparticles

Using a ceria-supported Pd catalyst obtained with the methodology described in Sec. IV, we simulate F adsorption as in Sec. V A. Figure 6 shows the heat of adsorption as a function of number of F atoms as they are incrementally added to the simulation. As the ceria support is generally free of defects, initially most of F adatoms are on the Pd nanoparticles. Also note the initial heat of adsorption has a value indicating much stronger adsorption for F than either Pd and ceria surface obtained in the section above. This is likely due to the presence of some very small Pd particles on the ceria support. As the number of F atoms increase, one starts to see some Ce atoms that are free of oxygen being lifted out the surface around the Pd-ceria interface. As more of the Ce atoms are reduced, the oxygen density on the surface increases. Eventually these oxygen atoms start to migrate towards the Pd nanoparticles and are ultimately chemisorbed on the Pd surface.

The hill-and-valley feature of differential heat of adsorption curve is sensitive to the F deposition rate used in the sim-

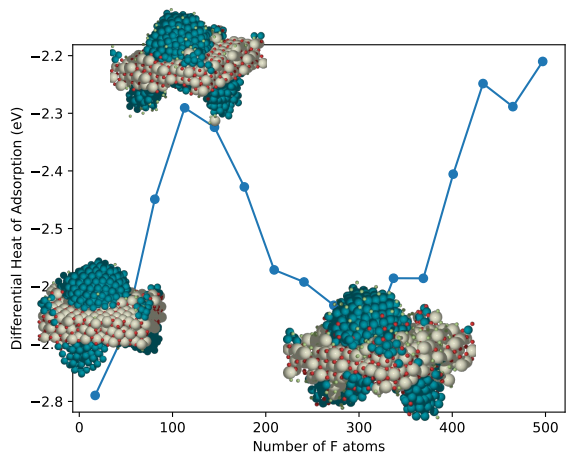


FIG. 6. The differential heat of adsorption for F on a ceria supported Pd nanoparticle, simulated at 800K with the number of F increases at a rate of 0.5 atom/ps. Insets show configurations when the number F atoms is 32, 128, and 320 respectively. The catalyst has a composition of  $Ce_{320}O_{640}Pd_{536}$  in a  $3.8 \times 3.8 \times 7.6nm^3$  simulation cell.

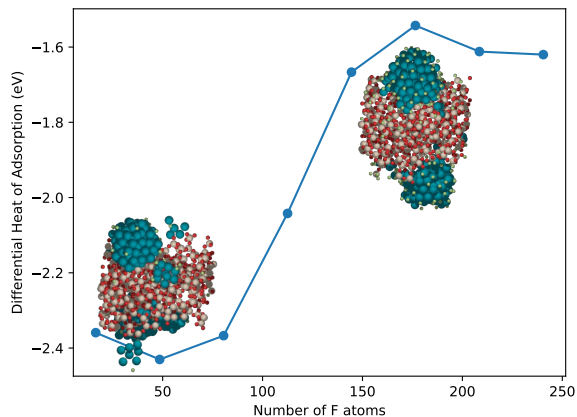


FIG. 7. The differential heat of adsorption for F on a silica supported Pd nanoparticle, simulated at 800K with the number of F increases at a rate of 0.25 atom/ps. Insets show configurations when the number F atoms is 48 and 192 respectively. The catalyst has a composition of  $Si_{300}O_{600}Pd_{253}$  in a  $3.0 \times 3.0 \times 6.0nm^3$  simulation cell.

ulations. The peak tends to shift to the left and flatten out as the deposition rate decreases. Thus, the feature indicates some activated or slow processes that delay the system from finding the more energetically favorable configurations. Here, we tentatively identify the rate limiting process for fluorine spillover from the Pd nanoparticle to ceria support as being the migration of oxygen from ceria to Pd. We are currently developing methodology to derive activation energy from MD simulations which should further clarify this issue.

Results for F deposition on a silica-supported Pd catalyst model is shown in Fig. 7. The differential heat of adsorption initially assumes the same value as for F/Pd, and become less negative as the F coverage increases due to repulsion between chemisorbed F adatoms, eventually reaching the value for F/silica obtained in Sec. V A. There is no big drop in the

curve as the case of Pd/ceria (cf. Fig. 6), consistent with the observation that no significant migration of oxygen from silica to Pd is observed. It is worth mentioning that when the number of F atoms is sufficiently high, F atoms do adsorb onto the silica surface, but only after Pd is fully covered by F. Thus we conclude from this MD study that spillover of F from Pd to silica is not significant.

## VI. CONCLUSION

Molecular dynamic simulations using machine learning potential trained by DFT data enable us to provide a truly dynamic picture of the migration of reactants during heterogeneous catalysis on supported nanoparticles, an important phenomena which is difficult to study theoretically with traditional methods. There are several novel applications of machine learning potentials here: a) preparing model surfaces using simulated annealing as catalyst supports; b) mimicking the formation of catalytic metal nanoparticles on model supports; and c) adsorption on catalyst surfaces and its study using the differential heat of adsorption. The latter constitutes an extension of an earlier study of S adsorption on coinage metal surfaces.<sup>20</sup>

Part of the motivation of this study is a previous experimental study<sup>21</sup> which shows that a ceria-supported Pd catalyst has exceptional ability to remove fluorine from fluorophenols (compared to Pd catalysts on other supports). Fluorine spillover from Pd to ceria support was conjectured from some preliminary MD studies to be one of the factors enabling this enhanced ability. The presence of fluorine on ceria have been verified experimentally.<sup>21</sup> In this study, we use a more realistic crystalline ceria substrate rather than an amorphous nanocluster used in the previous study, thus more realistically modeling the experiments. We suggest that the rate limiting process for spillover is likely to be the reverse migration of oxygen from the ceria support to the Pd nanoparticles.

The existence of potential complex synergetic effects involving supported metal nanoparticles, as well as the supports themselves, in catalytic processes means that traditional methods of separating complex systems to different components for analysis might not capture key aspects of behavior. In study of fluorine adsorption separately on Pd and ceria, no significant differences are found. Worse yet, using CeO<sub>2</sub>(111) as the substrate, even weaker F adsorption is found than on Pd. Only through MD studies using a ML potential, which can access time scales on the order of nanoseconds, is it revealed that migration of fluorine in this system is a result of the interplay between multiple elements. The ability of Pd to partially reduce ceria is crucial, especially at the later stages of the fluorine adsorption. By systematically comparing ceria and silica for their roles in fluorine adsorption, we also clarify why this is a unique feature of ceria, despite the fact that fluorine is known to also reduce silica.

Insights obtained from studies using the ML potential also identify the limitation and pitfalls of relying only on DFT calculations for modeling catalysis. Since the CeO<sub>2</sub>(111) surface is shown to be the most stable surface and is also ob-

served on ceria nanocubes in experiments, it is natural to use a CeO<sub>2</sub>(111) slab as a model surface for DFT studies. As mentioned earlier, the F adsorption energy is much weaker on a flat Ce<sub>2</sub>(111) surface than on Pd(111) surface, thus a standard DFT study will not reveal any F spillover on ceria supported Pd. One can systematically introduce defects such as steps and kinks, and even some amorphousness to the ceria model. However, one also needs to account for the energetics of the defects in addition to many different ways that fluorine can adsorb on those defects. Such a study is beyond the capability of typical DFT calculations, while machine learning potential is most suitable for this type of studies.

A recent experimental study<sup>33</sup> of Ir clusters on CeO<sub>2</sub>(111) thin films grown on a Cu(111) substrate is consistent with many of the findings of this work, including stability of nanoparticles and reverse oxygen spillover effects. It provides further indication that the use of ML potentials derived from DFT calculations can be a reliable method to study heterogeneous catalysis on supported nanoparticles.

## SUPPLEMENTARY MATERIAL

See the supplementary material for lists of systems used for training of the potentials, comparison between DFT and the ML potentials for select pairs of elements (Ce-O, Si-O, and F-Pd); and potential files for Ce-F-O-Pd and F-O-Pd-Si systems and input file for training.

## ACKNOWLEDGEMENTS

This work was supported for this work by the US Department of Energy, Office of Science, Basic Energy Sciences, Division of Chemical Sciences, Geosciences, and Biological Sciences, and was performed in the Computational and Theoretical Chemistry (CTC) project at Ames National Laboratory which is operated by Iowa State University under contract No. DE-AC02-07CH11358.

## DATA AVAILABILITY STATEMENT

The data that support the findings of this study are available within the article and its supplementary material.

<sup>1</sup>W. C. Conner and J. L. Falconer, "Spillover in heterogeneous catalysis," *Chemical Reviews* **95**, 759–788 (1995).

<sup>2</sup>W. Karim, C. Spreafico, A. Kleibert, J. Gobrecht, J. VandeVondele, Y. Ekinici, and J. A. van Bokhoven, "Catalyst support effects on hydrogen spillover," *Nature* **541**, 68–71 (2017).

<sup>3</sup>M. Xiong, Z. Gao, and Y. Qin, "Spillover in heterogeneous catalysis: New insights and opportunities," *ACS Catalysis* **11**, 3159–3172 (2021).

<sup>4</sup>G. M. Psofogiannakis and G. E. Froudakis, "DFT study of the hydrogen spillover mechanism on Pt-doped graphite," *The Journal of Physical Chemistry C* **113**, 14908–14915 (2009).

<sup>5</sup>A. Sihag, Z.-L. Xie, H. V. Thang, C.-L. Kuo, F.-G. Tseng, M. S. Dyer, and H.-Y. T. Chen, "DFT insights into comparative hydrogen adsorption and hydrogen spillover mechanisms of Pt<sub>4</sub>/graphene and Pt<sub>4</sub>/anatase (101) surfaces," *The Journal of Physical Chemistry C* **123**, 25618–25627 (2019).

- <sup>6</sup>J.-H. Guo, J.-X. Liu, H.-B. Wang, H.-Y. Liu, and G. Chen, “Combined DFT and kinetic Monte Carlo study of a bridging-spillover mechanism on fluorine-decorated graphene,” *Physical Chemistry Chemical Physics* **23**, 2384–2391 (2021).
- <sup>7</sup>W. Ji, N. Wang, X. Chen, Q. Li, K. Lin, J. Deng, J. Chen, and X. Xing, “Effects of subsurface oxide on Cu<sub>1</sub>/CeO<sub>2</sub> single-atom catalysts for CO oxidation: A theoretical investigation,” *Inorganic Chemistry* **61**, 10006–10014 (2022).
- <sup>8</sup>P. S. Rice and P. Hu, “Understanding supported noble metal catalysts using first-principles calculations,” *The Journal of Chemical Physics* **151**, 180902 (2019).
- <sup>9</sup>R. Ouyang, Y. Xie, and D.-E. Jiang, “Global minimization of gold clusters by combining neural network potentials and the basin-hopping method,” *Nanoscale* **7**, 14817–14821 (2015).
- <sup>10</sup>J. Timoshenko, D. Lu, Y. Lin, and A. I. Frenkel, “Supervised machine-learning-based determination of three-dimensional structure of metallic nanoparticles,” *The Journal of Physical Chemistry Letters* **8**, 5091–5098 (2017).
- <sup>11</sup>M. O. J. Jäger, E. V. Morooka, F. Federici Canova, L. Himanen, and A. S. Foster, “Machine learning hydrogen adsorption on nanoclusters through structural descriptors,” *npj Computational Materials* **4** (2018), 10.1038/s41524-018-0096-5.
- <sup>12</sup>N. Combe, P. Jensen, and A. Pimpinelli, “Changing shapes in the nanoworld,” *Phys. Rev. Lett.* **85**, 110 (2000).
- <sup>13</sup>K. C. Lai, Y. Han, P. Spurgeon, W. Huang, P. A. Thiel, D.-J. Liu, and J. W. Evans, “Reshaping, intermixing, and coarsening for metallic nanocrystals: Nonequilibrium statistical mechanical and coarse-grained modeling,” *Chemical Reviews* **119**, 6670–6768 (2019).
- <sup>14</sup>K. C. Lai, D.-J. Liu, and J. W. Evans, “Nucleation-mediated reshaping of faceted metallic nanocrystals: Breakdown of the classical free energy picture,” *The Journal of Chemical Physics* (2023), 10.1063/5.0138266.
- <sup>15</sup>J. Behler and M. Parrinello, “Generalized neural-network representation of high-dimensional potential-energy surfaces,” *Phys. Rev. Lett.* **98**, 146401 (2007).
- <sup>16</sup>A. P. Bartók, M. C. Payne, R. Kondor, and G. Csányi, “Gaussian approximation potentials: The accuracy of quantum mechanics, without the electrons,” *Phys. Rev. Lett.* **104**, 136403 (2010).
- <sup>17</sup>A. Thompson, L. Swiler, C. Trott, S. Foiles, and G. Tucker, “Spectral neighbor analysis method for automated generation of quantum-accurate interatomic potentials,” *Journal of Computational Physics* **285**, 316–330 (2015).
- <sup>18</sup>A. V. Shapeev, “Moment tensor potentials: A class of systematically improvable interatomic potentials,” *Multiscale Modeling & Simulation* **14**, 1153–1173 (2016).
- <sup>19</sup>L. Zhang, J. Han, H. Wang, R. Car, and W. E, “Deep potential molecular dynamics: A scalable model with the accuracy of quantum mechanics,” *Physical Review Letters* **120** (2018), 10.1103/physrevlett.120.143001.
- <sup>20</sup>D.-J. Liu and J. W. Evans, “Reaction processes at step edges on S-decorated Cu(111) and Ag(111) surfaces: MD analysis utilizing machine learning derived potentials,” *The Journal of Chemical Physics* **156**, 204106 (2022).
- <sup>21</sup>P. J. Naik, P. Kunal, D.-J. Liu, J. W. Evans, and I. I. Slowing, “Efficient transfer hydrodehalogenation of halophenols catalyzed by Pd supported on ceria,” *Applied Catalysis A: General* **650**, 119007 (2023).
- <sup>22</sup>See <https://www.vasp.at/> for general information of VASP.
- <sup>23</sup>J. P. Perdew, K. Burke, and M. Ernzerhof, “Generalized gradient approximation made simple,” *Phys. Rev. Lett.* **77**, 3865–3868 (1996), erratum-ibid. **78**, 1396 (1997).
- <sup>24</sup>H. Wang, L. Zhang, J. Han, and W. E, “DeePMD-kit: A deep learning package for many-body potential energy representation and molecular dynamics,” *Computer Physics Communications* **228**, 178–184 (2018).
- <sup>25</sup>A. Hjorth Larsen, J. Jørgen Mortensen, J. Blomqvist, I. E. Castelli, R. Christensen, M. Dułak, J. Friis, M. N. Groves, B. Hammer, C. Hargus, and et al., “The atomic simulation environment—a python library for working with atoms,” *Journal of Physics: Condensed Matter* **29**, 273002 (2017).
- <sup>26</sup>A. Jain, S. P. Ong, G. Hautier, W. Chen, W. D. Richards, S. Dacek, S. Cholia, D. Gunter, D. Skinner, G. Ceder, and K. A. Persson, “Commentary: The materials project: A materials genome approach to accelerating materials innovation,” *APL Materials* **1**, 011002 (2013).
- <sup>27</sup>M. Nolan, S. Grigoleit, D. C. Sayle, S. C. Parker, and G. W. Watson, “Density functional theory studies of the structure and electronic structure of pure and defective low index surfaces of ceria,” *Surface Science* **576**, 217–229 (2005).
- <sup>28</sup>A. Trovarelli and J. Llorca, “Ceria catalysts at nanoscale: How do crystal shapes shape catalysis?” *ACS Catalysis* **7**, 4716–4735 (2017).
- <sup>29</sup>R. Lawler, J. Cho, H. C. Ham, H. Ju, S. W. Lee, J. Y. Kim, J. II Choi, and S. S. Jang, “CeO<sub>2</sub>(111) surface with oxygen vacancy for radical scavenging: A density functional theory approach,” *The Journal of Physical Chemistry C* **124**, 20950–20959 (2020).
- <sup>30</sup>D. A. Siegel, W. C. Chueh, F. El Gabaly, K. F. McCarty, J. de la Figuera, and M. Blanco-Rey, “Determination of the surface structure of CeO<sub>2</sub>(111) by low-energy electron diffraction,” *The Journal of Chemical Physics* **139**, 114703 (2013).
- <sup>31</sup>N. T. Huff, E. Demiralp, T. Çagin, and W. A. Goddard III, “Factors affecting molecular dynamics simulated vitreous silica structures,” *Journal of Non-Crystalline Solids* **253**, 133–142 (1999).
- <sup>32</sup>L. C. Erhard, J. Rohrer, K. Albe, and V. L. Deringer, “A machine-learned interatomic potential for silica and its relation to empirical models,” *npj Computational Materials* **8** (2022), 10.1038/s41524-022-00768-w.
- <sup>33</sup>Y. Lykhach, J. Kubát, A. Neitzel, N. Tsud, M. Vorokhta, T. Skála, F. Dvořák, Y. Kosto, K. C. Prince, V. Matolín, V. Johánek, J. Mysliveček, and J. Libuda, “Charge transfer and spillover phenomena in ceria-supported iridium catalysts: A model study,” *The Journal of Chemical Physics* **151**, 204703 (2019).